A seesaw-lever force-balancing suspension design for space and terrestrial gravity-gradient sensing

Huafeng Liu, W. T. Pike, and Guangbin Dou

Citation: Journal of Applied Physics **119**, 124508 (2016); doi: 10.1063/1.4944709
View online: http://dx.doi.org/10.1063/1.4944709
View Table of Contents: http://aip.scitation.org/toc/jap/119/12
Published by the American Institute of Physics

A seesaw-lever force-balancing suspension design for space and terrestrial gravity-gradient sensing

Huafeng Liu,[a] W. T. Pike,[a] and Guangbin Dou
Optical and Semiconductor Devices Group, Department of Electrical and Electronic Engineering, Imperial College London, London SW7 2AZ, United Kingdom

(Received 15 January 2016; accepted 10 March 2016; published online 25 March 2016)

We present the design, fabrication, and characterization of a seesaw-lever force-balancing suspension for a silicon gravity-gradient sensor, a gravity gradiometer, that is capable of operation over a range of gravity from 0 to 1 g. This allows for both air and space deployment after ground validation. An overall rationale for designing a microelectromechanical systems (MEMS) gravity gradiometer is developed, indicating that a gravity gradiometer based on a torsion-balance, rather than a differential-accelerometer, provides the best approach. The fundamental micromachined element, a seesaw-lever force-balancing suspension, is designed with a low fundamental frequency for in-plane rotation to response gravity gradient but with good rejection of all cross-axis modes. During operation under 1 g, a gravitational force is axially loaded on two straight-beams that perform as a stiff fulcrum for the mass-connection lever without affecting sensitive in-plane rotational sensing. The dynamics of this suspension are analysed by both closed-form and finite element analysis, with good agreement between the two. The suspension has been fabricated using through-wafer deep reactive-ion etching and the dynamics verified both in air and vacuum. The sensitivity of a gravity gradiometer built around this suspension will be dominated by thermal noise, contributing in this case a noise floor of around $10\,\mathrm{E}/\sqrt{\mathrm{Hz}}$ ($1\,\mathrm{E} = 10^{-9}/\mathrm{s}^2$) in vacuum. Compared with previous conventional gravity gradiometers, this suspension allows a gradiometer of performance within an order of magnitude but greatly reduced volume and weight. Compared with previous MEMS gravity gradiometers, our design has the advantage of functionality under Earth gravity. © *2016 AIP Publishing LLC*. [http://dx.doi.org/10.1063/1.4944709]

I. INTRODUCTION

Gravity gradiometers have been developed to determine the gravity gradient for a number of terrestrial observations including oil and mineral exploration, crustal anomaly measurement and archaeology[1] since their first demonstration by Eotvos.[2] There are in general two types of gravity gradiometers categorized by whether the difference of gravitational forces is determined by the differential-accelerometer approach or the torsion-balance, as shown in Figure 1.

When frames are static, the most useful component of gravity gradient tensor Γ_{zz} can be determined by both approaches. For a differential-accelerometer-based gravity gradiometer, the two accelerometers directly determine the gravity gradient as the difference of the outputs divided by their separation. In contrast, the torsion-balance gravity gradiometer transduces the gravity gradient as a single measurement through coupling of two separated masses at either end of a centrally pivoted bar with the angular rotation proportional to the differential torque induced on the two masses by the gravity gradient. In this case, the sensitivity of the measurement will be related to the length of the bar rather than the separation of the two sensors in the differential-accelerometer approach. The output of this torsion-balance gradiometer is maximized when θ the angle between the bar and the gravity vector is 45°. A mechanical pathway from reference frames to the proof masses can be identified in both approaches, with the separation bar and flexures swapped in order, frame-bar-springs-masses for the differential-accelerometer and frame-spring-bar-masses for the torsion-balance.

Current gravity gradiometers, specified in Table I, use a combination of differential accelerometers[1,3–9] and torsion balance[10–15] approaches, with the former allowing injection of technology from accelerometer development, while the latter avoids the challenges of accommodating the large 1 g offset

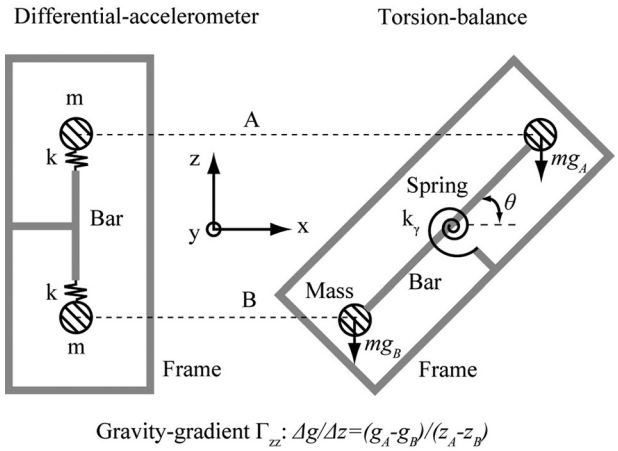

FIG. 1. A comparison of the principles of operation of differential-accelerometer and torsion-balance gradiometers for determining the vertical gravity-gradient component Γ_{zz} in an inertial frame.

[a]h.liu11@imperial.ac.uk and w.t.pike@imperial.ac.uk

TABLE I. Current conventional gravity gradiometers.

Company	Technology supplier	Principle	Gravity rejection	Noise floor	Tensor
BHP Billiton	Lockheed Martin	Diff.-Acc.	Rotation[3]	$3\,E/\sqrt{Hz}$	Partial
Bell Geospace	Lockheed Martin	Diff.-Acc.	Rotation[4]	$3\,E/\sqrt{Hz}$	Full
ARkeX	Lockheed Martin	Diff.-Acc.	Rotation[1]	$3\,E/\sqrt{Hz}$	Full
	University of Maryland	Diff.-Acc.	Supercon. magnetic levitation[5]	$1\,E/\sqrt{Hz}$	Γ_{zz}
AOSense	Stanford University	Diff.-Acc.	Free fall[9]	$24\,E/\sqrt{Hz}$	Full
Gedex	University of Maryland	Tor.-Bal.	Supercon. angular acc.[11]	$1\,E/\sqrt{Hz}$	Γ_{xx}, Γ_{yy}, Γ_{zz}
	University of West Australia	Tor.-Bal.	Supercon. angular acc.[13]	$1\,E/\sqrt{Hz}$	Γ_{zz}
Rio Tinto	University of West Australia	Tor.-Bal.	Supercon. angular acc.[14]	$1\,E/\sqrt{Hz}$	Γ_{zz}
Gravitec	University of West Australia	Tor.-Bal.	Resonating beam[15]	$5\,E/\sqrt{Hz}$	Γ_{xz}, Γ_{yz}

present in the vertical component of an acceleration. Such a challenge is met by differential accelerometer gradiometers using a variety of techniques. Lockheed Martin's gradiometer is continuously rotated to modulate the gravity signal and hence separate the signal from offset in frequency. Maryland's superconducting accelerometer is magnetically levitated to remove the gravity contribution, while Stanford University uses free fall in a similar manner. All three approaches require considerable extra mass and complexity. While torsion-balance approaches avoid dealing with the offset, the challenge is then transferred to their suspension as the flexural element should be sensitive to rotational motion but stiff to the translational gravity loading, requiring careful design to reject as far as possible any cross-axis contributions. As well as the vertical gravity component, any gradiometer has to reject other large signals due to measuring in a non-inertial frame: any measurement from the mobile deployment of a gradiometer has to strongly attenuate the external accelerations. A combination of sensor pairing, platform gimbling, and additional acceleration/rotational sensors has been used to separate the gravity gradient from the platform dynamics for both torsional and differential approaches. In addition, Lockheed Martin's rotation approach can also help attenuate the platform dynamics through oversampling of the external accelerations above the gravity gradient measurement bandwidth.

Due to the combined challenges of rejecting the gravity offset and platform dynamics, terrestrially deployed mobile gradiometers generally have a noise floor of $1\,E/\sqrt{Hz}$. In the microgravity environment of space, the offset problem no longer exists and existing gradiometers have therefore focused on differential accelerometers. In addition, on space platforms the external accelerations are greatly reduced. The highest performance achieved is by the Gravity field and steady-state Ocean Circulation Explorer (GOCE) satellite, launched in 2009. The core of the GOCE satellite is a differential-accelerometer-based gravity gradiometer which is comprised of three pairs of ultra-sensitive electrostatic accelerometers with a measurement range of only a few μg. With a resolution of $2\,pg/\sqrt{Hz}$, it can achieve a gravity gradient resolution of $4\,mE/\sqrt{Hz}$.[16] Recently, an airborne gravity gradiometer based on the GOCE accelerometers was introduced. GREMLIT[17] has four differential accelerometers providing a noise floor of $1\,E/\sqrt{Hz}$, demonstrating directly a performance degradation of approximately 250 in accommodating terrestrial gravity on a mobile platform.

II. PREVIOUS APPROACHES TO MINIATURIZE GRAVITY GRADIOMETERS

Conventional gravity gradiometers, whether based on differential accelerometry or torsion balance, range from 12 kg to several tons. Microelectromechanical systems (MEMS) technology offers the potential to miniaturise the sensors within the scaling laws of the transduction. Two approaches, one using differential accelerometry, the other torsion balance, have been presented. Flokstra[18] and co-workers used two identical accelerometers fabricated as a monolithic chip (80 mm × 80 mm) on a 100 mm silicon wafer. Each accelerometer has a large proof mass of 20 g, achieved by attaching gold blocks to the silicon. The masses are suspended by four spring beams and the displacement is sensed by gap-variation comb capacitive transducers. The resonant frequency of each accelerometer is around 1 Hz which at low temperatures and under vacuum theoretically corresponds to a noise floor of around $120\,mE/\sqrt{Hz}$. However, it is not possible to operate this suspension under 1 g and it has not been operated in a microgravity environment to date.

The second monolithic MEMS gravity gradiometer, based on the torsion-balance approach, has been developed by Ghose[19,20] and co-workers. Their first prototype had a short spring beam bridging the pivot anchor and the proof-mass pendulum and is sensitive to in-plane rotations. A second prototype has two spring beams suspending a mass pendulum and is sensitive to the out-of-plane rotations. Schematics of both prototypes, indicating the direction of the maximum sensing vector, are shown in Figure 2. The first prototype is fabricated on a SOI wafer allowing a proof mass of 600 μm thick, including the extra mass from the handle layer, giving a fundamental frequency of 1.35 Hz, while the second prototype is fabricated on a single silicon layer whose thickness is 130 μm, having a fundamental frequency of 1.5 Hz. The performance has not been reported for either prototypes, but based on the proof mass, resonance, and a Q of 100 000, a noise floor of 5 and $11\,E/\sqrt{Hz}$ can be derived. Both prototypes have their displacements sensed by gap-variation capacitive transducers in their compliant directions, and this limits their range as the capacitive gap must be maintained within tight tolerances. However, a more important limitation of both designs is that the gravity vector is transverse to the rotational flexure, inducing off axis displacements. The first design had a considerable out-of-plane sag displacement of 15 μm under Earth gravity, resulting in misalignment and spurious vibration issues. In

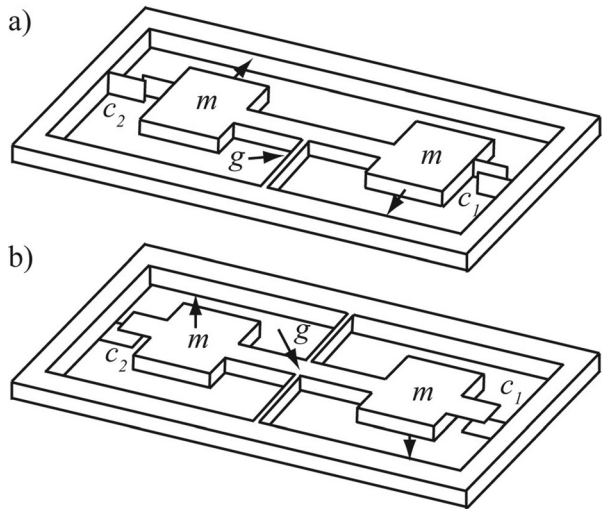

FIG. 2. Schematics showing the operating principles of EPFL's monolith MEMS gravity gradiometers based on the torsion-balance approach[20] both with gap-variation differential capacitive sensing. The gravity vector, g, is shown with the proof masses labelled m and the capacitive transducers c_1 and c_2.

order to overcome these issues, the second prototypes were designed to reduce the out-of-plane sag. While this design is directed to operation in a microgravity environment, the flexure is still not optimised for rejecting terrestrial gravity.

The aim of this work is to identify a design pathway for a MEMS gravity gradiometer, capable of operation on both Earth and in a microgravity environment, with a performance noise floor below $10\,\mathrm{E}/\sqrt{\mathrm{Hz}}$. We achieve this in four steps. First, we determine which of the two approaches, differential accelerometry or torsion balance, provides the optimum MEMS solution. Second, we design a suspension with the fundamental and cross axis stiffness that will allow operation under a range from 0 to 1 g, within the design rules that our microfabrication imposes. Third, we fabricate the suspension using through-wafer etching. Finally, we confirm the dynamics of the fabricated suspension in air and in vacuum to determine the fundamental performance noise floor of our approach. This paper provides a complete description of the design methodology, dynamics, and characterization briefly described for a previous higher-resonant-frequency prototype.[21]

III. DESIGN REQUIREMENTS

The first step is to compare the two possible approaches, differential-accelerometer and torsion-balance, in terms of their performance floor. This floor is determined by the sum of all the noise contributions. At the sensor level, the two major contributions are from the thermal noise of the suspension and the electronics noise from the transduction of the proof-mass motion, whether in translation or rotation. To aid comparison, we ignore details of the implementation in the first instance and assume that the resonant frequencies ω_0 and quality factors Q of the both approaches are the same, as are their displacement-transducer noise floor, N_{DT}, their temperature, T, proof masses, m, and the separation of the proof masses, d. In this case, the electronics noise floor, N_{elec}, of each sensor will be

$$N_{elec}(diff) = N_{DT}{\omega_0}^2 \tag{1}$$

and

$$N_{elec}(tor) = 2N_{DT}{\omega_0}^2/d. \tag{2}$$

The thermal noise floor will be

$$N_{therm}(diff) = \sqrt{\frac{4k_bT\omega_0}{mQ}} \tag{3}$$

and

$$N_{therm}(tor) = \sqrt{\frac{8k_bT\omega_0}{mQd^2}}. \tag{4}$$

Performing as gravity gradiometers, their total equivalent noise of gravity gradient will be

$$N_{gg}(diff) = \frac{1}{d}\sqrt{2\left(N_{therm}(diff)^2 + N_{elec}(diff)^2\right)} \tag{5}$$

and

$$N_{gg}(tor) = \sqrt{N_{therm}(tor)^2 + N_{elec}(tor)^2}. \tag{6}$$

Substituting (5) and (6) to (3) and (4) shows the equivalent noise of gravity gradient for both methods is the same $N_{gg}(diff) = N_{gg}(tor)$.

In both cases, the ratio of the contributions for thermal and electronic noises of the order

$$\left(\frac{N_{therm}}{N_{elec}}(diff)\right)^2 = \frac{4k_bT}{{\omega_0}^3{N_{DT}}^2mQ} \tag{7}$$

and

$$\left(\frac{N_{therm}}{N_{elec}}(tor)\right)^2 = \frac{2k_bT}{{\omega_0}^3{N_{DT}}^2mQ}. \tag{8}$$

These ratios are of the same order and can be quantified for a MEMS sensor. A N_{DT} of $1\ \mathrm{pm}/\sqrt{\mathrm{Hz}}$ has been demonstrated for MEMS sensors,[22] while a resonance of 1.3 Hz is achievable with a proof mass of 1 g ($20 \times 20 \times 0.5$ mm silicon). A Q of 100 000 can be obtained in vacuum. Hence for $T = 80\,\mathrm{K}$, $\omega_0 = 10\,\mathrm{rad/s}$, $N_{DT} = 1\,\mathrm{pm}/\sqrt{\mathrm{Hz}}$, $m = 1\,\mathrm{g}$, and $Q = 100\,000$, this gives a ratio for both methods in the order of 1×10^7, indicating that the thermal noise floor will dominate, independent of the details of our initial assumptions.

In summary, the total noise of differential-accelerometer and torsion-balance approaches is the same and is dominated by the thermal noise. However, the performance under the Earth's gravitational field produces different challenges to the two approaches. For differential accelerometry, the gravitational field has to be rejected using rotation, levitation, or free fall, each with a considerable resource overhead and a MEMS solution would offer marginal gains. In contrast, the torsion balance approach transfers the problem of field rejection to the suspension and transducers. Here, the micromachining of

silicon might offer some distinct advantages: the flexures and proof masses are fabricated monolithically from a single crystal, ensuring that minimal stresses are produced during manufacture and no creep occurs afterwards. This opens up the possibility of a design that exploits the predictability of the stresses in a MEMS suspension to control its response under gravity. Having selected a torsion-balance approach, consider the best geometry that takes advantage of a MEMS approach.

IV. GRADIOMETER DESIGN

A. Overall sensor geometry

The critical aspect of the design is that the gradiometer should be able to sense the vertical component of the gravity gradient Γ_{zz} within Earth's gravitational field. While the gravity-gradient torque moves the two proof masses in opposite directions, under the gravity field they also move in parallel. This puts demands on both the suspension and the transduction. The cross-axis stiffness, expressed as the ratio of the cross-axis translational mode along the gravity vector to the fundamental rotational mode about the pivot, should be as high as possible. At the same time, the rotation transducer has to sense motion about the horizontal pivot while being able to accommodate a cross-axis gravitational field and reject motion in that direction.

In order to meet the demands on the flexure, a seesaw-lever force-balancing suspension has been designed to allow rotation in-plane for gravity gradient sensing and stiff to gravity loading. The maximum cross-axis stiffness is achieved by putting the flexures of the suspension into axial tension under gravity such that the restoring forces can act directly to increase the stiffness without, to the first order, increasing the fundamental frequency, performing as a fulcrum. An orthogonal set of four flexures allows operation for all orientation angles about the sensing pivot axis. Figure 3 shows schematically such a set of flexures in the xy plane about a central pivot point providing full support of the proof mass under gravity. In contrast, the flexures of the designs for earlier work in Figure 2 provide no axial tension in the gravity direction allowing sag in the proof mass that complicates operation under a range of gravitational fields.

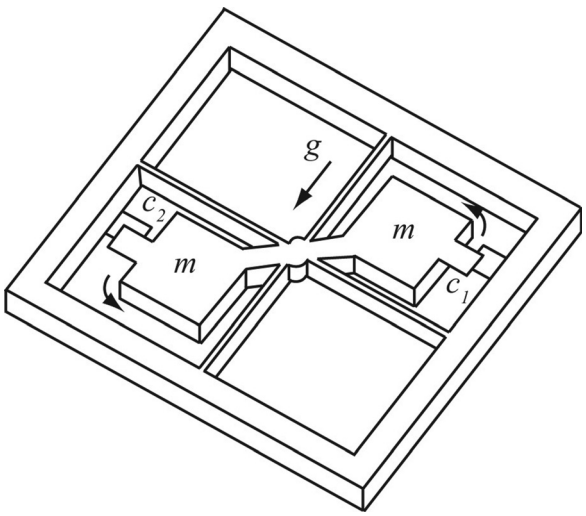

FIG. 3. Schematic of the MEMS gravity gradiometer design with a seesaw-lever force-balancing suspension allowing area-variation differential capacitive sensing.

With the geometry of the suspension of the gradiometer defined, the motion that should be transduced is an in-plane rotation about the pivot, while the in-plane sag under gravity, already minimised by the suspension, should be accommodated while minimising its transduction. A lateral capacitive array transducer (LCAT)[22] offers a possible solution, with the output dependent on the change in overlap between a series of moving electrodes on the two proof masses and a corresponding series of fixed electrodes on a facing die. A noise floor of $1\,\mathrm{pm}/\sqrt{\mathrm{Hz}}$ is achievable with a $12\,\mu$m gap between the moving and fixed electrodes, with a lateral separation of around $12\,\mu$m. Control of the gap is maintained by maximising the stiffness of the suspension to translation in the z axis as well as rotations about the x and y axes.

B. Mass distribution consideration

The mass distribution should be chosen to get maximum performance from a given die. Within a square die, an angular accelerometer can utilise the entire area as an inertial mass. However, a gradiometer can only use one half of the xy plane as only two quadrants will contribute a gravity gradiometer torque (GGT) of the same polarity. Figure 4 shows the two possible symmetries that allocate the proof mass areas in the required opposing quadrants in a die plan, with the die perimeter shown as a dotted line. Both die plans, labelled bow-tie and checker-board, can be arranged in a space-filling packing of a wafer, as indicated.

The choice between the two geometries is made by maximising the performance, determined by the minimum noise, for a given die area. The thermal noise equivalent angular acceleration (TNEAA) of a torsion-balance gravity gradiometer is

$$TNEAA = \sqrt{\frac{4k_bT\omega_0}{I_{zz}Q}}, \tag{9}$$

where I_{zz} is the moment of inertia.

If thermal noise sets the performance floor, assuming the two dies have the same Q and area, this performance parameter is very similar for both dies, with the bow-tie

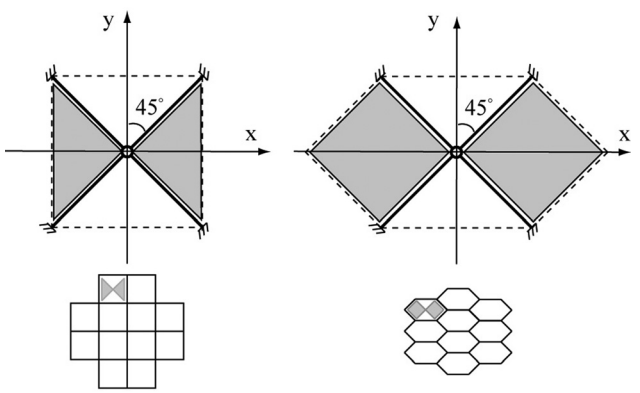

a) Bow-tie geometry b) Checker-board geometry

FIG. 4. Schematics of the gradiometer geometry plan.

geometry 5% better. However, if the electronics noise sets the performance floor, the performance depends on the product of the gravity-torque displacement response and the maximum possible capacitance of the angular transducer, with the latter term reflecting that the input gain to the electronics is limited by any stray capacitance. In this case, the performance therefore depends directly on the product of the gravity-gradient-torque sensitivity, the resonant frequency, and the first moment of area of the proof mass about the pivot. Calculating those product for the two geometries, the checker-board will be seven times better, and so a better choice where electronics noise dominates.

Hence, to optimise the performance for potential testing in air, where the electronics noise dominates, we have selected the checker-board geometry. This choice comes at a minimal cost for the evacuated case where the checker-board geometry will be within 5% of the optimum performance.

C. Suspension dynamics

A model gradiometer design of the checker-board geometry, including the support frames, is shown in Figure 5. A series of four beam flexures, each of length L, width w, and thickness t, allow a rotation of the proof-mass pair, each of size $a \times a$, about the z axis with the rotation angle, γ, proportional to the gravity gradient along $x = y$. A circular area, of radius r, is allocated as a central link between the suspension and proof masses. For a beam geometry of $w \ll L$ and for small deflections of the flexure less than w, the standard cantilever equations can be used to provide an analytical solution for the suspension dynamics.

1. Fundamental rotation mode

The pivot is guided to rotate in the xy plane by the four flexures and the dynamics can be treated as a two dimensional. Figure 6 further simplifies the treatment for the balance of forces for a single flexure, with the effect of the other three flexures reflected as the boundary condition of a pivot point with a new set of axes, u and v axial and transverse to the flexure. An applied torque T_γ about this pivot point is balanced by a beam-bending moment which consists of both the torque from the end force F_v with a torque arm of l_{arm} and the force couple M_γ

$$T_\gamma = F_v l_{arm} + M_\gamma. \tag{10}$$

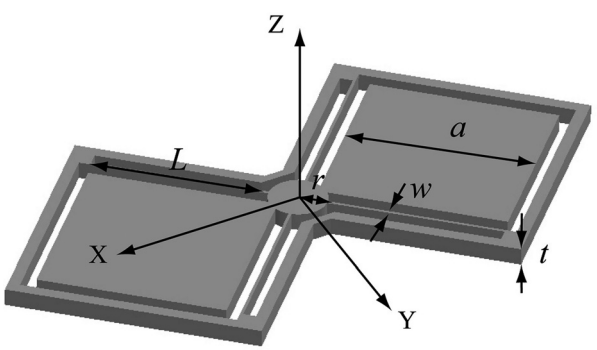

FIG. 5. Schematic of the MEMS gravity gradiometer prototype.

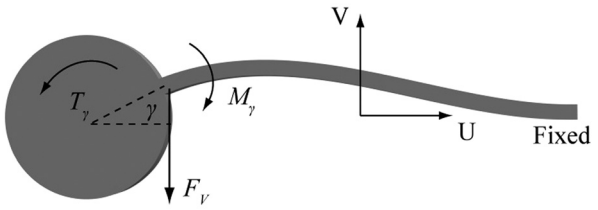

FIG. 6. Fundamental rotation mode: the beam has its one end guided to rotate in-plane with the other end fixed.

Assuming the spring deformation is within its elastic range, the dynamics can be solved by the stiffness matrix method,[23] $\mathbf{F} = \mathbf{K} \cdot \mathbf{D}$ giving

$$\begin{bmatrix} F_u \\ F_v \\ M \end{bmatrix} = \begin{bmatrix} \frac{EA}{L} & 0 & 0 \\ 0 & \frac{12EI_z}{L^3} & \frac{6EI_z}{L^2} \\ 0 & \frac{6EI_z}{L^2} & \frac{4EI_z}{L} \end{bmatrix} \begin{bmatrix} u \\ v \\ \gamma \end{bmatrix}, \tag{11}$$

where E is the Young's modulus, L is the beam length, A is the beam cross-sectional area, and $I_z = w^3 t/12$ is the second moment of area. The end force and the force couple moment can be directly derived as

$$F_v = \frac{12EI_z}{L^3} v + \frac{6EI_z}{L^2} \gamma \tag{12}$$

and

$$M_\gamma = \frac{6EI_z}{L^2} v + \frac{4EI_z}{L} \gamma. \tag{13}$$

Based on the Hook's law, the torque applied on the pivot is equivalent to product of the rotational spring constant of a single beam k_γ' and the rotation angle γ, having $T_\gamma = k_\gamma' \gamma$. For small deflections $u = 0$ and $v = r\gamma$, the dynamics reduce to a single degree of freedom in γ with a corresponding four-beam spring constant of

$$k_\gamma = \frac{4Ew^3 t}{3L}\left(1 + \frac{3r}{L}\right), \tag{14}$$

for small r/L

$$= \frac{4Ew^3 t}{3L}. \tag{15}$$

The angular frequency of the fundamental rotation mode is given by

$$\omega_\gamma^2 = \frac{k_\gamma}{I_{zz}} = \frac{8Ew^3}{7\rho L a^4}\left(1 + \frac{3r}{L}\right), \tag{16}$$

where $I_{zz} = 7\rho t a^4/6$ is the moment of inertia of the proof mass pair about the pivot.

2. Cross-axis translation along gravity mode

During operation, the designed gradiometer should sit vertically for sensing vertical gravity gradient Γ_{zz}. Hence,

this sensor has to accommodate a vertical displacement. If the sag induced beam deformation is substantial, the dynamic characterization of the gradiometer will be compromised. To avoid this effect, the suspension stiffness for vertical direction should be as large as possible.

In this design, the gradiometer sits vertically for sensing vertical gravity gradient along u-axis, shown in Figure 7. This vertical sag mode is defined as the xy translational mode since u- or v-axis is 45° between x- and y-axis. The total stiffness along this direction is comprised of lateral stiffness k_v and axial stiffness k_u for two beams each. But the lateral stiffness of thin beam is much smaller than its axial stiffness; therefore, the in-plane cross-axis stiffness can be simplified

$$k_{xy} = 2k'_u + 2k'_v \approx 2k'_u = \frac{2Ewt}{L}, \tag{17}$$

the simple expression for the axial stiffness of the two identical flexure in parallel.

Hence, the squared angular frequency of this mode is

$$\omega_{xy}^2 = \frac{k_{xy}}{m} = \frac{Ew}{\rho La^2}. \tag{18}$$

The axial loading effect under Earth gravity will not affect the gradiometer dynamic characterization since the axial stiffness of the suspension beams is much larger than others. This is also verified by simulations later. Hence, these two axial-loaded beams perform as the fulcrum of the seesaw-lever force-balancing suspension.

3. Cross-axes rotational modes

The two lowest-frequency spurious modes correspond to rotations about the x- or y-axis. The four flexures in this mode enforce a pivot along the x- or y-axis through the centre of the link cylinder (Fig. 8). These modes are three dimensional with the flexure both twisting axially and deflecting out of the xy plane.

The sum of the torques at the inner base of flexure gives

$$T_\varphi \varphi = M_\eta \eta + M_\xi \xi + F_z \Delta z, \tag{19}$$

where $T_\varphi = k'_\varphi \varphi$ is the exerted torque. The stiffness matrix method can again be applied, but in this case using the full three-dimensional components.[23] This gives the out-of-plane force F_z and torques M_η, M_ξ, as

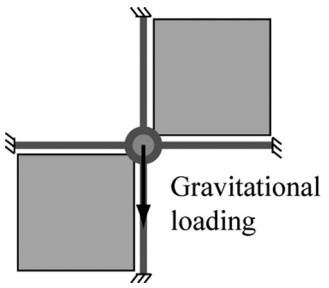

FIG. 7. Gravity gradient sensing mode under gravity.

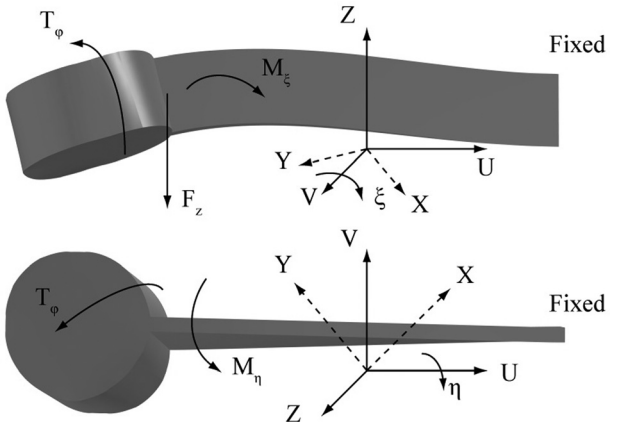

FIG. 8. Cross-axis rotation around x- or y-axis with an angle of φ (Fig. 9).

$$F_z = \frac{12EI_v}{L^3} z - \frac{6EI_v}{L^2} \xi, \tag{20}$$

$$M_\eta = \frac{GJ}{L} \eta, \tag{21}$$

and

$$M_\xi = \frac{4EI_v}{L} \xi - \frac{6EI_v}{L^2} z, \tag{22}$$

where GJ is the torsional rigidity of a thin beam. According to the gradiometer geometry, the angles of η, ξ about u- and v-axis are both equal to $\varphi \cos 45°$, and the out-of-plane deflection $z = \eta r + \xi t(1 - \cos \xi)$ (Fig. 9). Assuming small rotational angles and a link radius much smaller than the flexure length, and a large aspect ratio for the beam, as can be obtained in MEMS fabrication with $w \ll t$, the two modes can be derived as

$$\omega_\alpha^2 = \frac{k_\varphi}{I_{xx}} = \frac{4Ewt^2}{\rho La^4} \left(1 - \frac{3r}{L}\right) \tag{23}$$

and

$$\omega_\beta^2 = \frac{k_\varphi}{I_{yy}} = \frac{2Ewt^2}{3\rho La^4} \left(1 - \frac{3r}{L}\right). \tag{24}$$

4. Out-of-plane translational mode

The out-of-plane translational mode (Fig. 9) will be important for fabrication robustness and to control the transducer geometry. Following the stiffness matrix method, the out-of-plane stiffness of the four-beam suspension system is

$$k_z = \frac{4Ewt^3}{L^3}, \tag{25}$$

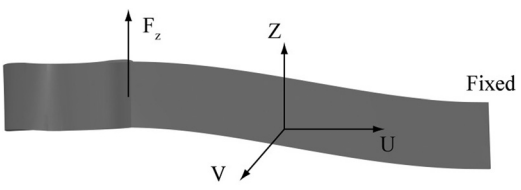

FIG. 9. Out-of-plane translational mode.

and the squared angular frequency is equal to

$$\omega_z^2 = \frac{k_z}{m} = \frac{2Ewt^2}{\rho L^3 a^2}. \quad (26)$$

5. Spurious mode rejection ratios

The rejection ratio between spurious resonant frequencies and the fundamental frequency should be as large as possible. Assuming the pivot radius r is much smaller than the spring beam length L and the side length of the square mass a is comparable with the spring length L, the resonant frequencies and rejection ratios can be approximately expressed in Table II. The theoretical model considers the material as isotropic for the first order approximation. The rejection ratios are dependent on the MEMS fabrication, namely, the aspect ratio of the springs, t/w, and the die size to beam width L/w.

6. Finite element analysis (FEA) simulations

A commercial FEA software COMSOL Multi-physics has been used to validate the dynamics of the gradiometer design. Figure 10 illustrates simulation results of the first four vibration modes of the gradiometer in three dimensions. The fundamental mode is rotating in plane about z-axis. The first and third spurious modes are cross-axis rotations about principle y- and x-axis, respectively. The out-of-plane translational vibration mode is the second spurious mode.

FEA simulations for the fundamental frequency of the gradiometer were performed with four parameters: the beam width $w = 20\,\mu$m, the beam length $L = 14$ mm, the pivot radius $r = 0.3$ mm, and the mass side-length $a = 14$ mm. Comparison of closed-form solutions and FEA are plotted in Figure 11. FEA simulation results agree well with the theoretical results.

Figure 12 plots the variation of the rejection ratios with the beam width. Again, the FEA simulations have good agreement with the theoretical results.

V. FABRICATION IMPLEMENTATION

To validate the dynamic characteristics of the gradiometer suspension design, deep reactive-ion etching (DRIE) was used to fabricate silicon devices for preliminary testing. The whole-processes were depicted in Figure 13, using a double-side

TABLE II. Closed-form solutions of the gradiometer suspension.

Mode	Expression	Rejection ratio	Value
$\omega_\gamma^2 = \frac{k_\gamma}{I_{zz}}$	$\frac{8E}{7\rho}\frac{w^3}{L^5}\left(1+\frac{3r}{L}\right)$	$\frac{f_\gamma}{f_\gamma}$	1
$\omega_{xy}^2 = \frac{k_{xy}}{m}$	$\frac{E}{\rho}\frac{w}{L^3}$	$\frac{f_{xy}}{f_\gamma}$	$\sqrt{\frac{7}{8}}\frac{L}{w}$
$\omega_\beta^2 = \frac{k_\varphi}{I_{yy}}$	$\frac{2E}{3\rho}\frac{wt^2}{L^5}\left(1-\frac{3r}{L}\right)$	$\frac{f_\beta}{f_\gamma}$	$\sqrt{\frac{7}{12}}\frac{t}{w}$
$\omega_z^2 = \frac{k_z}{m}$	$\frac{2E}{\rho}\frac{wt^2}{L^5}$	$\frac{f_z}{f_\gamma}$	$\sqrt{\frac{7}{4}}\frac{t}{w}$
$\omega_\alpha^2 = \frac{k_\varphi}{I_{xx}}$	$\frac{4E}{\rho}\frac{wt^2}{L^5}\left(1-\frac{3r}{L}\right)$	$\frac{f_\alpha}{f_\gamma}$	$\sqrt{\frac{7}{2}}\frac{t}{w}$

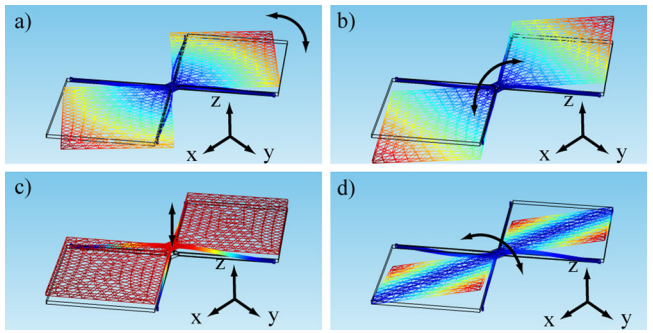

FIG. 10. First four vibration modes of the gradiometer in COMSOL: (a) the fundamental mode γ about z-axis, (b) the first spurious mode β about y-axis, (c) the second spurious mode z along z-axis, and (d) the third spurious mode α about x-axis.

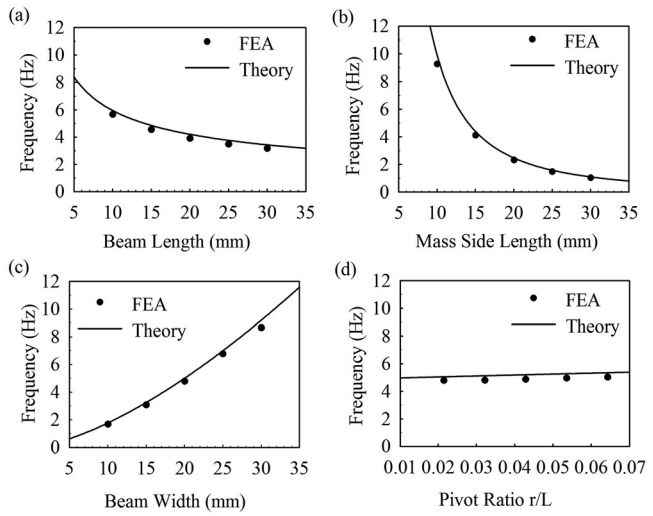

FIG. 11. Variation of the fundamental frequency with (a) the beam width w, (b) the beam length L, (c) the ratio of the pivot radius to the beam length r/L, and (d) the mass side length a, from FEA (points) and stiffness matrix analysis (lines).

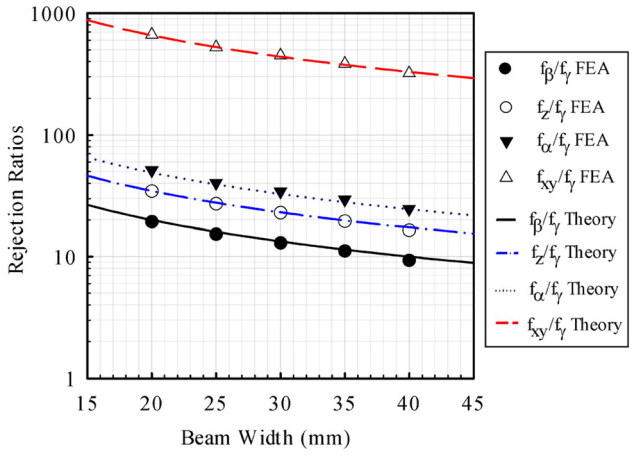

FIG. 12. Rejection ratios of spurious modes to the fundamental mode as a function of the beam width.

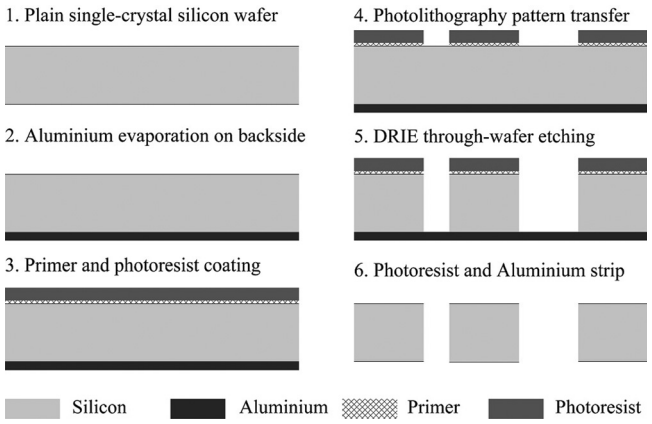

FIG. 13. DRIE through-wafer fabrication flow.

polished 4-in. single-crystal silicon wafer with a thickness of 525 μm. First, an aluminium layer of around 400 nm was evaporated on the back side of the silicon wafer to alleviate notching during DRIE through-wafer etching. After a dehydration process, a photoresist layer was coated on the primer prepared wafer surface. The wafer was exposed by ultraviolet (UV) light under a photomask. After the development in the developer, the etching windows were opened and ready for DRIE. After through-wafer etching, the top photoresist and bottom aluminium layers were striped by soaking the etched wafer in acetone and then developer.

A fabricated gradiometer prototype alongside a British pound is shown in Figure 14. The two 15 mm square proof-masses, in total 0.55 g, are connected by a 1 mm pivot radius suspended by four 26 μm wide and 14 mm long beams connecting to the outer frame.

VI. SUSPENSION DYNAMICS CHARACTERIZATION

A. Experiment setup

The dynamics of the prototype was measured by a commercial laser displacement sensor Keyence LK-G5000 series with a resolution of 25 nm for the laser head LK-H052.[24] The basis of displacement measurements is triangulation[25] from laser reflection on a CMOS image sensor (Fig. 15). For excitation, a piezoelectric diaphragm was driven by a function generator. Both passive and active anti-vibration stages were used to suppress the background vibration noise.

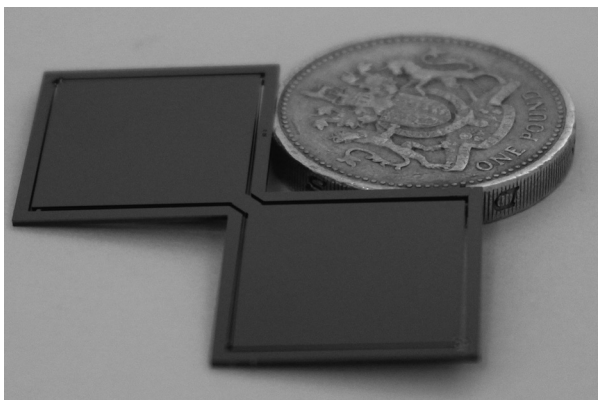

FIG. 14. Fabricated MEMS gravity gradiometer prototype on a British pound.

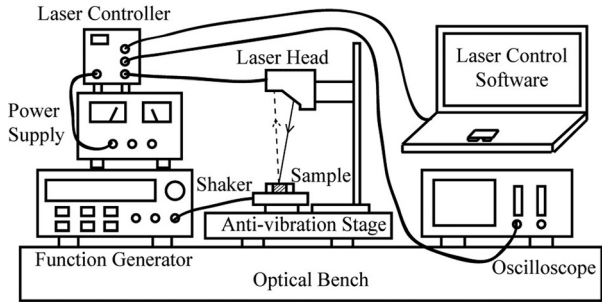

FIG. 15. Characterization setup for validating gravity gradiometer suspension dynamics.

The frame of the gradiometer prototype was fixed on a customized glass holder, enabling the gradiometer suspension free to move. The laser beam was vertically directed at the gradiometer proof-mass. A thin gold layer was plated on the top of the prototype to improve the reflected power.

B. Experimental results

For the fundamental frequency measurement, the gradiometer was excited by rotating it in-plane manually. Due to the uneven gold features, the laser head can sense the distance difference. In this case, the position of the reflected laser spot on CMOS varied periodically during the in-plane vibration of the gradiometer. Once the excitation force was absent, the gradiometer would oscillate at its fundamental frequency. Hence, the measured displacement-variation frequency of the laser spot can be used to determine the fundamental frequency of the gradiometer.

In order to measure other vibration modes, the glass holder was fixed on the piezoelectric diaphragm driven by a sinusoidal signal sweeping from 10 Hz to 300 Hz. Once the signal frequency was close to one of the gradiometer resonant frequencies, the vibration amplitude became evident and was then detected by the laser displacement sensor. Hence, the resonant frequencies of the gradiometer were investigated by observing maximum achievable amplitudes while sweeping the frequency of the signal generator. In this case, the first four resonant frequencies of the gradiometer were found and their power spectrum is plotted in Figure 16. The measured

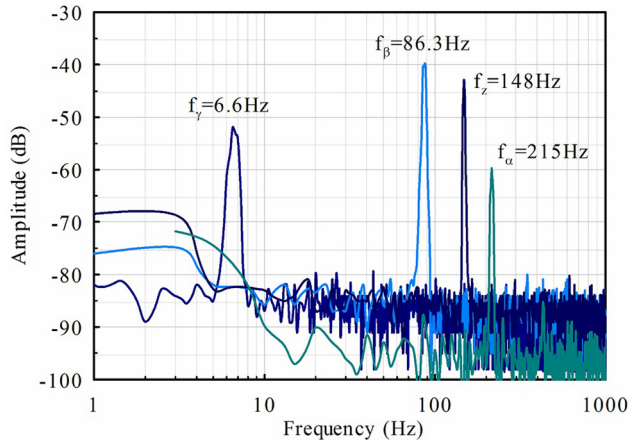

FIG. 16. Resonant frequencies distribution of the gravity gradiometer by different excitation frequencies and amplitudes.

TABLE III. Suspension characterization results comparison.

Mode	FEA	Closed-form	Measurement
f_γ(Hz)	6.3	7.0	6.6
f_β(Hz)	89.8	86.3	86.3
f_z(Hz)	158.6	180.8	148.1
f_α(Hz)	242.8	211.6	215.2
f_{xy}(Hz)	2820	3410	…
Rejection ratio	…	…	…
f_β/f_γ	14.3	12.4	13.1
f_z/f_γ	25.2	26.0	22.4
f_α/f_γ	38.5	30.4	32.6
f_{xy}/f_γ	447	487	…

results are compared with theoretical and FEA simulation results in Table III.

A typical ring-down experiment was conducted to investigate the quality factor of the gradiometer operated in air. The results are plotted in Figure 17. The vibration amplitude decayed exponentially, and the decay time constant was measured as 17.5 s, giving a quality factor of 360 in air. Hence, the thermal noise can be calculated from Equation (9) as $160\,\mathrm{E}/\sqrt{\mathrm{Hz}}$ at room temperature in air.

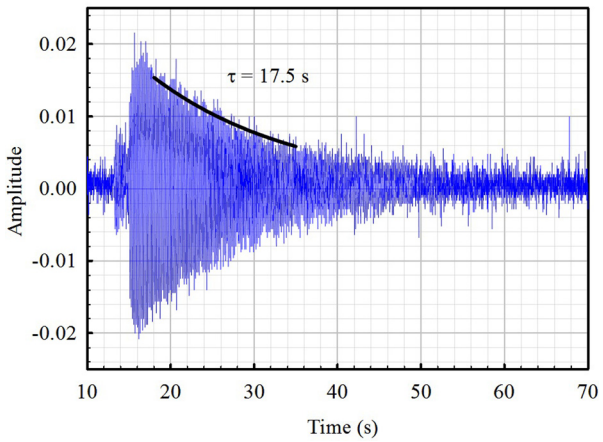

FIG. 17. Ring-down experiment of the gradiometer in air.

VII. DISCUSSION

The frequency of the cross-axis translational mode is more than 400 times larger than the in-plane mode, corresponding to a sag displacement under Earth gravity of 20 nm. Hence, the displacement transducer geometry is unaffected by the external gravity environment. In order to quantify the effect of gravity on the dynamics, FEA was used to determine that the fundamental mode with and without gravity shifts by just 3 ppm. With its suspension cable of providing excellent rejection of the gravitational field, the gradiometer can operate in a full range of gravity environments.

For the inertial platform of a space deployment, a single device of the current design can be used to determine one component of the gravity gradient tensor. To provide common-mode rejections of rotations about the suspension pivot axis that can be expected on a dynamic platform, two identical devices can be monolithically fabricated in an orthogonal orientation on a single chip.

The suspension of Figure 14 can be vacuum packaged between two capping dies. For the critical device dimension of 12 μm, the mean free path corresponds to a pressure of 2000 Pa. Hence, a relatively modest vacuum will eliminate gas damping, typically allowing a Q of 100 000. This corresponds to a thermal noise floor of $10\,\mathrm{E}/\sqrt{\mathrm{Hz}}$ at room temperature. The electronics for the gradiometer displacement transducer we are going to use are inherited from the NASA's InSight microseismometer which has been developed recently in our group.[22] The estimated electronic noise is negligible, around $0.2\,\mathrm{E}/\sqrt{\mathrm{Hz}}$ for our gradiometer design. The total noise floor of our MEMS gravity gradiometer would be $10\,\mathrm{E}/\sqrt{\mathrm{Hz}}$ listed in Table IV. Compared with predictions from previous MEMS gravity gradiometers with the same quality factor, temperature and similar die size, our MEMS sensor has a comparable noise floor and can also be operated on Earth. Compared with conventional gravity gradiometers in Table I, the performance of our MEMS sensor is within an order of magnitude but greatly reduced volume and weight.

VIII. CONCLUSION

We have presented a rationale for optimising the geometry of a MEMS gravity gradiometer capable of operation under a range of gravity environments. The design and dynamical analysis of a seesaw-lever force-balancing suspension for a torsion-balance gravity gradiometer has been developed to identify and maximally reject all cross-axis modes, with closed-form and FEA results in good agreement. The suspension has been fabricated using a DRIE through-wafer process and the analysis validated against sensor performance. The noise floor of a MEMS gravity gradiometer based on this suspension is derived as $10\,\mathrm{E}/\sqrt{\mathrm{Hz}}$, within an order of magnitude than conventional gravity gradiometers and comparable to previous MEMS gravity gradiometers.

TABLE IV. The pivot is guided to rotate performance comparisons of MEMS gravity gradiometers.

Gradiometer Units	Mass (g)	I_{zz} (kg m^2)	Die area (mm^2)	Dies (-)	f_0 (Hz)	Therm. noise (E/$\sqrt{\mathrm{Hz}}$)	Elect. noise (E/$\sqrt{\mathrm{Hz}}$)	Total noise (E/$\sqrt{\mathrm{Hz}}$)	Op. on Earth (-)
This work	0.55	7.2×10^{-8}	650	6	6.6	10	0.2	10	Yes
Ghose[20]	0.1	1.3×10^{-8}	760	6	1.5	11[a]	…	>11	No
Ghose[19]	0.33	6.9×10^{-8}	1200	4	1.4	5[a]	…	>5	No
Flokstra[18]	20	…	6400	1	1	0.2[a]	0.05	0.2	No

[a]Derived from given parameters.

ACKNOWLEDGMENTS

We would like to thank Professor Andrew Holmes for valuable discussions, and Dr. M. Ahmad, Dr. A. K. Delahunty, and Dr. A. Mukherjee for fabrication suggestions.

[1]D. DiFrancesco, A. Grierson, D. Kaputa, and T. Meyer, "Gravity gradiometer systems–advances and challenges," Geophys. Prospect. **57**, 615–623 (2009).
[2]L. Bod, E. Fischbach, G. Marx, and M. Naray-Ziegler, "One hundred years of the eötvös experiment," Acta Phys. Hung. **69**, 335–355 (1991).
[3]J. B. Lee, "Falcon gravity gradiometer technology," Explor. Geophys. **32**, 247–250 (2001).
[4]C. A. Murphy, "The air-FTG airborne gravity gradiometer system," in *Airborne Gravity 2004–Abstracts from the ASEG-PESA Airborne Gravity 2004 Workshop: Geoscience Australian Record* (2004), Vol. 18, pp. 7–14.
[5]J. Lumley, J. White, G. Barnes, D. Huang, and H. Paik, "A superconducting gravity gradiometer tool for exploration," in *Airborne Gravity* (2004), pp. 21–40.
[6]H. Chan and H. Paik, "Superconducting gravity gradiometer for sensitive gravity measurements. I. Theory," Phys. Rev. D **35**, 3551 (1987).
[7]H. Chan, M. Moody, and H. Paik, "Superconducting gravity gradiometer for sensitive gravity measurements. II. Experiment," Phys. Rev. D **35**, 3572 (1987).
[8]M. Moody, H. Chan, and H. Paik, "Superconducting gravity gradiometer for space and terrestrial applications," J. Appl. Phys. **60**, 4308–4315 (1986).
[9]X. Wu, "Gravity gradient survey with a mobile atom interferometer," Ph.D. thesis (Stanford University, 2009).
[10]R. L. Forward, "Electronic cooling of resonant gravity gradiometers," J. Appl. Phys. **50**, 1–6 (1979).
[11]M. Annecchione, M. Moody, K. Carroll, D. Dickson, and B. Main, "Benefits of a high performance airborne gravity gradiometer for resource exploration," in *Proceedings of Exploration 07: Fifth Decennial International Conference on Mineral Exploration* (2007).
[12]M. Moody, "A superconducting gravity gradiometer for measurements from a moving vehicle," Rev. Sci. Instrum. **82**, 094501 (2011).
[13]R. Matthews, "Mobile gravity gradiometry," Ph.D. thesis (University of Western Australia, 2003).
[14]J. Anstie, T. Aravanis, M. Haederle, A. Mann, S. McIntosh, R. Smith, F. Van Kann, G. Wells, and J. Winterflood, "Vk-1-a new generation airborne gravity gradiometer," in *ASEG Extended Abstracts* (CSIRO Publishing 2009), pp. 1–5.
[15]A. Veryaskin, "A novel combined gravity and magnetic gradiometer system for mobile applications," in *2000 SEG Annual Meeting* (2000).
[16]M. Fehringer, G. Andre, D. Lamarre, and D. Maeusli, "A jewel in ESA's crown," in *ESA Bulletin* (2008), pp. 14–23.
[17]K. Douch, B. Christophe, B. Foulon, I. Panet, G. Pajot-Métivier, and M. Diament, "Ultra-sensitive electrostatic planar acceleration gradiometer for airborne geophysical surveys," Meas. Sci. Technol. **25**, 105902 (2014).
[18]J. Flokstra, R. Cuperus, R. Wiegerink, and M. van Essen, "A MEMS-based gravity gradiometer for future planetary missions," Cryogenics **49**, 665–668 (2009).
[19]K. Ghose and H. Shea, "Fabrication and testing of a MEMS based earth sensor," in *IEEE Transducers* (2009), pp. 327–330.
[20]K. Ghose, "MEMS inertial sensor to measure the gravity gradient torque in orbit," Ph.D. thesis (EPFL, 2012).
[21]H. Liu, W. T. Pike, and G. Dou, "Design, fabrication and characterization of a micro-machined gravity gradiometer suspension," in *IEEE Sensors* (2014), pp. 1611–1614.
[22]W. T. Pike, A. K. Delahunty, A. Mukherjee, G. Dou, H. Liu, S. Calcutt, and I. Standley, "A self-levelling nano-g silicon seismometer," in *IEEE Sensors* (2014), pp. 1599–1602.
[23]C. Dym, *Structural Modeling and Analysis* (Cambridge University Press, 1997).
[24]Keyence, LK H052 User Manual, 2014.
[25]Keyence, LK G5000 Series User Manual 2014.